Ultrasensitive Resonant Electrometry Utilizing Micromechanical Oscillators

Dongyang Chen,[1,2] Hemin Zhang,[2] Jiangkun Sun,[2] Milind Pandit,[2] Guillermo Sobreviela,[2] Yong Wang,[1] Qian Zhang,[1] Xuying Chen,[1] Ashwin Seshia,[2] and Jin Xie[1,*]

[1] *State Key Laboratory of Fluid Power and Mechatronic Systems, Zhejiang University, Hangzhou 310027, People's Republic of China*

[2] *The Nanoscience Centre, Department of Engineering, University of Cambridge, Cambridge CB3 0FF, United Kingdom*

(Received 30 July 2019; revised 15 May 2020; accepted 15 June 2020; published 1 July 2020)

Real-time monitoring of minute quantities of charge plays an important role in quantum-physics research and electrical measurements within modern high-end scientific instruments. High-precision charge detection approaching the single-electron level at room temperature in analog or digital electronics is limited due to the considerable thermal noise. Herein, we propose a method of charge measurement with a resolution of 0.17 e/$\sqrt{\text{Hz}}$ at room temperature by resonant electrometry based on tracking the quasidigital frequency output of a highly force-sensitive oscillator. Real-time charge monitoring by 67 electrons per step is performed. We demonstrate a charge prebiased scheme for physically manipulating the quadratic nature of charge sensing of the oscillator into parabolic and linear forms with dramatic improvements in metrics such as sensitivity and resolution. Theoretical models for describing the underlying physics of both the charge measurement and resolution amplification schemes are established and validated. Due to the high quality factor of the resonator, the theoretical limit for the charge-input referred noise of the electrometer induced by thermomechanical noise is estimated in the order of 10^{-4} e/$\sqrt{\text{Hz}}$. This study also provides insights of resonant sensing applied to the next generation of electrometers and associated instrumentation systems.

DOI: 10.1103/PhysRevApplied.14.014001

I. INTRODUCTION

Quantization of charge is defined by the elementary charge carried by an individual proton or electron. The unbalanced quantities of electrons and protons in various physical entities, such as nuclear particles, ionic compounds, and biomacromolecules, produce electropositive or electronegative characteristics as a measurable physical property. The accurate measurement of charge is thus of significant interest. An electrometer is an instrument that can precisely measure small quantities of electric charge. Therefore, electrometers play an important role in scientific research, such as biological and chemical charge detection [1], quantum and nuclear physics [2], mass spectrometry [3], scanning tunneling microscopy [4], and space exploration [5]. Electrometers can also be employed in the instruments that require electrical measurements, e.g., multimeters, due to the fact that electrical parameters, such as voltage or current, can be indirectly inferred from charge measurements.

To date, high-precision electrometry has had a long history and a variety of macro and micro electrometers with different kinds of charge-measurement schemes have been developed [6–27], dating back from Coulomb's torsion-balance electrometer more than 200 years ago to transistors, carbon nanotubes, and quantum-dot devices, etc. Metallic single-electron transistors, such as aluminum-based devices, have demonstrated manipulation and detection of single electrons, approaching metrological accuracy of 0.5 part per 10^6 [6,7]. Alternatively, the semiconductor-based counterparts, such as using gallium arsenide with two-dimensional electron gas, have demonstrated relative benefits of fabrication simplicity and higher sensitivities by incorporating quantum dots with single-electron transistors [8–11]. A further concept of a mesoscopic charge sensor is that of quantum-point contacts [12,13], where conductance changes through the contacts pertaining to input charge are detected. Due to the underlying physical mechanisms involving Coulomb blockade and single-electron tunneling, these devices have limited dynamic range. Another limitation for high-precision charge detection at electron level in analog and digital electronics is the considerable thermal noise at room temperature. The use of analog devices for electrometry, e.g., transistors, suffers from electronic noise generated from many sources, especially the thermal noise that suppresses the fundamental charge-sensing principle of Coulomb blockade. One solution [8–12] for this is cryogenically cooling, which

*xiejin@zju.edu.cn

also limits the development of practical general-purpose instrumentation and commercialization. Nanomechanical electrometers can perform ultrasensitive charge measurement approaching quantum limits but still require operating temperatures below 4.2 K [15,16].

To meet the requirements of portable and cost-effective real-world electrometry applications, a concept of resonator-based electrometers [17–27] for measuring charge quantities at the electron level at room temperature involving the utilization of resonators as the core sensitive component, has been proposed based on micro electromechanical system (MEMS) and nanoelectromechanical system (NEMS) technologies. These electrometers convert the perturbation from input charge to a change in the output signal of externally driven resonators, e.g., measured by amplitude, phase, or frequency. In such a context, mechanical resonators are preferred due to the excellent quality factor they offer, exceeding the electronic counterparts by several orders of magnitude [30,31]. Three types of electrometers monitoring different output metrics from the resonators have been reported. The vibrating reed electrometers [17–20] utilize resonance motion to generate variable capacitances that modulate input charge to a voltage output at twice that of the operating frequency of the resonator. This property enables the electrometers to run the detection at a higher frequency thus reducing the effect of low-frequency noise, such as $1/f$ noise. In order to achieve high sensitivity, a large capacitance for modulating charge is required, which in turn causes significant on-chip capacitive parasitics, which leads to charge leakage and thus inaccuracy of detection. Recently, a fabrication process based on silicon on glass instead of conventional silicon on insulator has been reported to minimize inherent parasitic capacitances and enhance charge resolution to 1.03 e/$\sqrt{\text{Hz}}$ [20]. Mode-localized electrometers boost charge sensitivity by hundreds of times in terms of the output metric of amplitude ratio based on the principle of vibration energy localization between weakly coupled mechanical resonators [21–23]. Yet, the charge resolution is limited by considerable amplitude noises from each individual resonator. For this reason, the best resolution reported is 9.21 e/$\sqrt{\text{Hz}}$ [23]. Besides, the output metric of amplitude ratio has nonlinear errors in measurement range caused by inherent dynamics [28,29], which limits the measurement range.

The limitations in vibrating reed and mode-localized cases can be addressed in the metrology of resonant electrometry, which refers to tracking frequency change of the resonator to probe charge on an integrated electrode [24–27]. The reasons are (1) the gate capacitance for measuring charge is expected to be as small as possible so that the input charge can generate a large electrostatic force to increase sensitivity; this can avoid large parasitics; (2) the core oscillators are usually operated in the resonant regime where frequency output are better decoupled from amplitude noise. Resonant MEMS electrometry has previously been implemented by an axial strain modulation scheme [24–26], where the charge-induced electrostatic force is applied along the axial direction of a vibrating beam resonator. This method is less sensitive compared to the above-mentioned approaches, and is unable to identify positive and negative charge polarities.

In this work, we demonstrate the charge measurement by room-temperature resonant electrometry based on frequency modulation of a micromechanical oscillator with resolution beyond a single electron. A highly sensitive charge-detection scheme that uses stiffness perturbation on modal vibration of an oscillator is implemented. The monitoring on output metric of quasidigital resonant frequency of the oscillator offers ultrahigh stability with sub-1-ppb level of precision while the same level of precision in tracking voltage or current for the analog counterparts is a challenge. We further demonstrate a charge prebiased scheme to manipulate the quadratic nature of charge-frequency conversion to parabolic and linear forms with dramatic amplifications on sensitivity and resolution. The prototype resonant electrometer has a resolution of 0.17 e/$\sqrt{\text{Hz}}$, exceeding the best reported result of 16 250 e/$\sqrt{\text{Hz}}$ when compared to other counterparts of resonant electrometry [22,24–27] at room temperature. Additionally, the charge polarity can be distinguished. The proposed device has high resolution and large dynamic range while preserving the merits of low cost and low-power consumption as well as implementation in a standard microfabrication process [32].

II. MODELING

Fabrication of the resonant electrometer is completed by using a SOI wafer consisting of a 25-μm-thick phosphorus-doped highly conductive (n-type) single-crystal silicon device layer topping on a 2-μm-thick oxide layer and a 400-μm-thick handle layer, as shown in Fig. 1(a). The detailed fabrication process is described in our previous work [33]. The vibratory element on the silicon device layer consists of a singly anchored circular beam (SACB) with the other end set free. We use varying capacitance as the electromechanical coupling mechanism for read-out of the motion response from the SACB. Symmetric parallel-plate capacitors are formed by sandwiching the attached plate of the SACB between the driving and sensing electrode and are used for capacitively driving the SACB into resonance. In the meantime, the resonance motion is monitored by detecting the varying-capacitance-induced motional current output from the sensing electrodes. As a result of spurious mode suppression by symmetric actuation, SACB is deterministically operated at an elastic mode deformed with elliptical shape, as depicted in Figs. 1(b) and 2(a). The gate capacitor is formed by placing the free end of the SACB beside the charge-input gate electrode

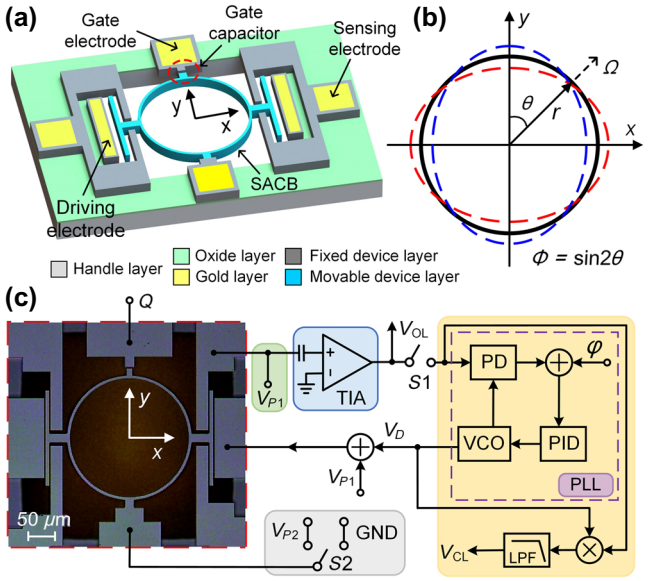

FIG. 1. (a) Design illustration of the prototype micromechanical resonant electrometer. The gold layer is used for wire bonding the device with the drive and read-out circuits implemented on a printed circuit board. (b) Schematics of the elliptical mode shape of the circular beam resonator in the established polar coordinate system. The blue and red dashed lines show the resonant motion of SACB with elliptical mode shape while the black solid line represents the position of equilibrium. (c) Optical micrograph of the mechanical electrometer showing the silicon device layer consisting of movable and fixed structures, and the experimental implementations for open-loop and closed-loop operation.

with a 2.5-μm gap. When small quantities of charge are applied on the gate electrode, an electrostatic attractive force is generated across the gap of the gate capacitor [see Figs. 2(a) and 2(b)]. The SACB will experience this charge-induced force during resonant motion and the natural frequency varies in response to this force. From this viewpoint, we build a sensitivity model for describing charge-frequency conversion in the resonator.

The resonator can be considered as an undamped spring-mass vibration system, as modeled in Fig. 2(b). In order to analyze the vibration behavior, a polar coordinate system $(r,\ \theta)$ is established, as shown in Fig. 1(b), where r is the radius and θ is the polar angle. The x and y axes are aligned with the directions of resonator actuation and charge perturbation, respectively. In the case of a thin circular beam where the midsurface radius is much larger than the radial width (the width of the beam in radial direction), the elliptical mode shape Φ becomes independent of the midsurface radius and can be described by an angular position-dependent function $\Phi(\theta) = \sin 2\theta$. Thus, the time-varying displacement Ω of the circular beam is given by $\Omega(t,\ \theta) = \Lambda(t) \times \Phi(\theta)$, where t is the time and $\Lambda(t)$ is the generalized time-dependent modal coordinate. The motions at different angular positions of the circular beam are all assumed to be harmonic and given by $\Lambda(t) = A\sin(2\pi f_N t + \varphi)$, where A is the vibration amplitude at the natural frequency f_N and φ is the phase determined by the original state of the resonator. Accordingly, we model the vibration system as single-degree-of-freedom differential equation of motion using Lagrange's method, and obtain

$$\frac{d}{dt}\left(\frac{\partial U_K}{\partial \dot{\Lambda}}\right) - \frac{\partial U_K}{\partial \Lambda} + \frac{\partial U_P}{\partial \Lambda} = 0, \tag{1a}$$

$$U_P = \frac{EI}{2R^3}\int_0^{2\pi}\left(\Omega + \frac{\partial^2 \Omega}{\partial \theta^2}\right)^2 d\theta, \tag{1b}$$

$$U_K = \int_0^{2\pi}\frac{1}{2}\rho w h\left(\frac{\partial \Omega}{\partial t}\right)^2 d\theta + \sum_j \frac{1}{2}m_j\left(\frac{\partial \Omega(\theta_j)}{\partial t}\right)^2, \tag{1c}$$

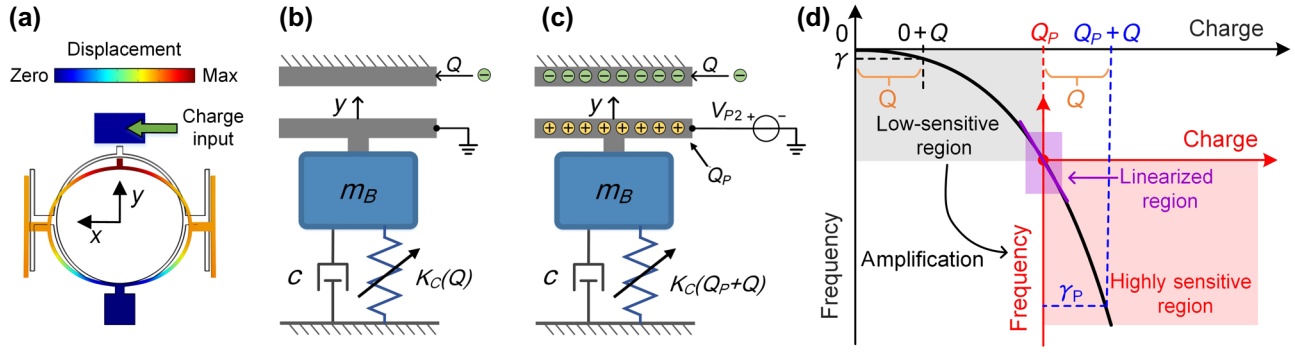

FIG. 2. (a) Mode shape of the SACB from finite-element simulation. Spring-damper-mass vibration system for describing the resonating circular beam under the stiffness perturbation by charge input on the gate capacitor (b) without and (c) with charge (Q_P) prebiased scheme. In the simplified calculation of undamped assumption, the damping coefficient $c = 0$. (d) Illustration of the sensitivity and resolution amplification of the charge prebiased scheme based on the quadratic sensitivity curve of the stiffness perturbation charge-sensing scheme. The coordinate system with the black arrow line corresponds to the original stiffness perturbation scheme in (b) while the inside coordinate system with the red arrow line corresponds to the measurement under charge prebiased states in (c).

where U_P and U_K are the potential energy and kinetic energy of the system. E and ρ are the elastic modulus and material density with values of 169×10^9 Pa and 2330 kg/m^3 for single-crystal silicon. I is the moment of inertia. For a rectangular cross section of the beam, we get $I = hw^3/12$. R, w, and h are the midsurface radius, radial width and thickness of the circular beam with values of 127.3, 5, 25 μm. m_j denotes the attached mass on the beam at different angular positions θj. In this case, the two attached masses are at the nodes with maximal displacement, which yields $\sum m_j = 2.57 \times 10^{-10}$ kg. Given that $\Phi(\theta)$ is time independent and $\Lambda(t)$ is position independent, Eq. (1) can be further deduced as

$$m_B \ddot{\Lambda} + K_B \Lambda = 0, \tag{2a}$$

$$K_B = \frac{d^2 U_P}{d\Lambda^2} = \frac{EI}{2R^3} \int_0^{2\pi} \left(\Phi + \frac{\partial^2 \Phi}{\partial \theta^2} \right)^2 d\theta, \tag{2b}$$

$$m_B = \frac{d^2 U_K}{d(\partial \Lambda / \partial t)^2} = \int_0^{2\pi} \rho w h \Phi^2 d\theta + \sum_j m_j \Phi(\theta_j)^2, \tag{2c}$$

where K_B and m_B are the mechanical stiffness and effective mass of the SACB. Substituting the harmonic motion term $\Lambda(t)$ to Eq. (2a), the natural frequency f_N of the resonator can be derived as $f_N = \sqrt{K_B/m_B}/2\pi$. Under the electrostatically forced vibration, as shown in Fig. 1(c) where an ac voltage V_D ($V_D \ll V_{P1}$) is applied to provide dynamic force for driving the SACB in the vicinity of the natural frequency while a dc bias voltage V_{P1} is used to polarize the parallel-plate capacitors for electromechanical coupling, an electrical stiffness K_E is introduced to the system as we have analyzed in Refs. [34,35], given by $K_E = -4\varepsilon_0 S_P {V_{P1}}^2/g^3$, where ε_0 is the dielectric constant with value of 8.85×10^{-12} F/m under vacuum; S_P and g are the plate area and gap distance of the parallel-plate capacitors with values of 4200 μm^2 and 3 μm. As shown in Fig. 2(b), given that the vibration amplitude A of the elliptical mode shape along y direction is much smaller in comparison to the gap distance of the gate capacitor $G = 2.50$ μm, at the maximal mechanical displacement, the potential energy change U_C to the vibration system while charge (Q) to be detected through loading on the gate capacitor is given by

$$U_C = \frac{G^2}{2\varepsilon_0 S_C} \int_{-A}^{A} \frac{Q^2}{(G+y)^2} dy, \tag{3a}$$

$$K_C(Q) = \frac{d^2 U_C}{dA^2} = -\frac{Q^2}{\varepsilon_0 S_C G}, \tag{3b}$$

where $K_C(Q)$ denotes the perturbed stiffness to the resonator deduced from the displacement derivative of U_C. S_C is the plate area of the gate capacitor with a value of 300 μm^2. Equation (3b) indicates that the charge-perturbed stiffness is independent of vibration amplitude. Combining all the equations above, we derive the frequency response $f_C(Q)$ of the resonator under charge perturbation as follows:

$$f_C(Q) = \frac{1}{2\pi} \sqrt{\frac{K_B + K_E + K_C(Q)}{m_B}} = f_R \sqrt{1 + \frac{K_C(Q)}{K_B + K_E}}, \tag{4}$$

where f_R is the resonant frequency under forced vibration and zero charge input. By expanding Eq. (4) into Taylor series, the relative frequency change γ is given by

$$\gamma = \frac{f_C(Q) - f_R}{f_R} = -\frac{Q^2}{2\varepsilon_0 S_C G (K_B + K_E)}. \tag{5}$$

Accordingly, a relative charge sensitivity Γ can be calculated as $\Gamma = \gamma/Q^2 = -250.60$ ppb/fC^2 using the given parameters while V_{P1} is fixed at 20 V. Equation (5) describes the quadratic nature of the charge detection by stiffness perturbation scheme. Based on that, we further propose a sensitivity amplification to the charge measurement by introducing charge prebiased states to the gate capacitor. To carry out the charge prebiased scheme, *S2* is switched to connect with V_{P2} and meanwhile V_{P1} is disabled so that the resonator is polarized on the SACB. In this case, the gate capacitor is precharged by V_{P2}, leading to a prebiased charge Q_P on the gate capacitor, given by $Q_P = \varepsilon S_C V_{P2}/G$, as can be seen in Figs. 2(b) and 2(c), which clearly depicts the difference between the situations of stiffness perturbation without and with charge prebiased scheme. By taking this prebiased state as outset, the new relative frequency shift in response to charge addition is given by

$$\gamma_P = \frac{f_C(Q_P + Q) - f_C(Q_P)}{f_C(Q_P)} = \sqrt{1 + \frac{K_C(Q_P + Q) - K_C(Q_P)}{K_B + K_E + K_C(Q_P)}} - 1. \tag{6}$$

From Eq. (3), we obtain $K_C(Q_P + Q) = -(Q_P + Q)^2/\varepsilon_0 S_C G$. By substituting that into Eq. (6) and then expanding Eq. (6) into Taylor series with higher-order terms neglected, we obtain

$$\gamma_P = \frac{-Q^2 + 2Q_P Q}{2\varepsilon_0 S_C G [K_B + K_E + K_C(Q_P)]}. \tag{7}$$

As can be seen, the charge prebiased scheme increases the original quadratic sensitivity into a parabolic sensitivity by adding a linear term $2QQ_P$. Notice that, under the original stiffness perturbation scheme described by Eq. (5), either

positive or negative charge leads to downward frequency shift. However, with the prebiased states, given that Q_P is positive, the charge polarity can be distinguished. The resonant frequency shifts upward and downward when measuring positive and negative charge, respectively. While $Q_P \gg Q$, neglecting the Q^2 term in the numerator of Eq. (7) only causes a negligible measurement error. Assuming that error is less than 1‰, we have $Q^2/2QQ_P < 1‰$. Subsequently, we can get $Q_P/Q > 500$ and this relation can be easily satisfied when the charge quantities to be measured are ranged from single electron to hundreds of electrons. In terms of $Q_P \gg Q$ at the prebiased states, we linearize the relative sensitivity Γ_P as follows:

$$\Gamma_P = \frac{\gamma_P}{Q} = \frac{2Q_P}{2\varepsilon_0 S_C G[K_B + K_E + K_C(Q_P)]}, \quad (Q_P \gg Q). \tag{8}$$

Equation (8) models a linearized region where frequency linearly shifts against input charge. By comparing Eqs. (8) and (5), we can get $\Gamma_P \approx 2Q_P \times \Gamma$, which indicates that, in the linearized region, Q_P functions as an amplification factor to the charge sensitivity.

To intuitively illustrate the underlying mechanism, we plot the sensitivity curve of the stiffness perturbation scheme, which shows a quadratic relation between the frequency variations and input charge on the coordinate system with black arrow line in Fig. 2(d). The sensitivity amplification benefits from the quadratic nature of the charge sensitivity where dramatic changes in frequency response occur at a region with large quantities of input charge. With charge prebiased states, the outset for charge measurement changes, for example, to the origin of the new coordinate system with the red arrow line. Strengthening charge prebiased states functions as moving the measurement along the quadratic curve to a more highly sensitive region. Thus, the relative sensitivity is significantly boosted and meanwhile can be linearized around the offset point set by the charge prebiased scheme when measuring charge quantities at the electron level. The linearized region expands with the increase of Q_P. The amplification factor is determined by the quadratic charge sensitivity Γ and the prebiased charge Q_P. According to the theoretical model and designed parameters, while 42.48fC quantities of Q_P is precharged on the gate capacitor, Γ_P can reach 3.50 ppb/e. For mechanical oscillators with high quality factor, sub-1-ppb frequency stability is achievable [36] so that the resonant electrometry utilizing mechanical oscillators can achieve charge resolution beyond single electron.

III. VERIFICATION

The experimental setup for the resonant electrometer is shown in Fig. 1(c), where two implementations, viz. the open loop and closed loop for the purposes of electrometry function verification and tracking of the frequency output in real time, are shown. Firstly, we validate the theory of charge detection by the stiffness perturbation scheme. In that case, the main body of the circular beam is grounded by switching *S2* to ground (GND). By enabling $V_{P1} = 20$ V, the resonator is polarized on the driving and sensing electrodes. By passing through a transimpedance amplifier (TIA), the motion-induced motional current from the sensing electrodes is amplified as V_{OL}, which is the output in open loop while *S1* is switched off. To close the loop, we switch *S1* on to feedback V_{OL} to a phase-locked loop (PLL). Within the PLL, the phase of V_{OL} is detected by a phase detector (PD) for feeding to a proportional-integral-derivative (PID) controller to enable control on a voltage-controlled oscillator (VCO) to output V_D as the driving signal with shifted phase by φ. Therefrom, we can precisely control the phase difference φ between V_{OL} at the output port of the resonator and V_D at the input port. The Barkhausen criteria are satisfied and a stable oscillation can be achieved to output the resonant frequency in real time. The oscillation amplitude and frequency are demodulated as V_{CL} for output. The prototype electrometer is tested at room temperature and in a vacuum chamber with pressure level under 20 mTorr. For the calibration of charge sensitivity, we use voltage and current source to generate and maintain known quantities of static and flowing charge Q on the gate capacitor, respectively. The quantities of input charge are determined by current integrating over time for current source and by multiplication of step voltage and the gate capacitance C_g for voltage source. C_g can be determined by finite-element simulation using the geometric parameters mentioned above, e.g., the plate area S_C and gap distance G, and the dielectric constant under vacuum $\varepsilon_0 = 8.85 \times 10^{-12}$ F/m. In this case, C_g is found as 1.06 fF.

We map the frequency spectra of the electrometer in both open and closed loop in response to different quantities of charge on the gate capacitor, as shown in Fig. 3. In the open-loop test, the spectral responses under forward- and backward-frequency sweep in the absence of input charge are consistent, which indicates that the resonator works in the linear regime. The resonant frequency is found to be 143 029 Hz with an offset phase of 52°, matching the theoretical result of 142 ± 2 kHz calculated by Eq. (4). The error estimate of ± 2 kHz is subject to 1% fabrication error in dimensions of the circular beam, e.g., the radical width and midsurface radius, which are the most possible error sources that affect the resonant frequency. In closed-loop operation, by locking phase difference of the input and output ports at different values, the corresponding oscillation frequencies and amplitudes are recorded as shown in the dot plot, which are also consistent to the results from open-loop test. This clearly shows good oscillation tracking function of our control loop. Then

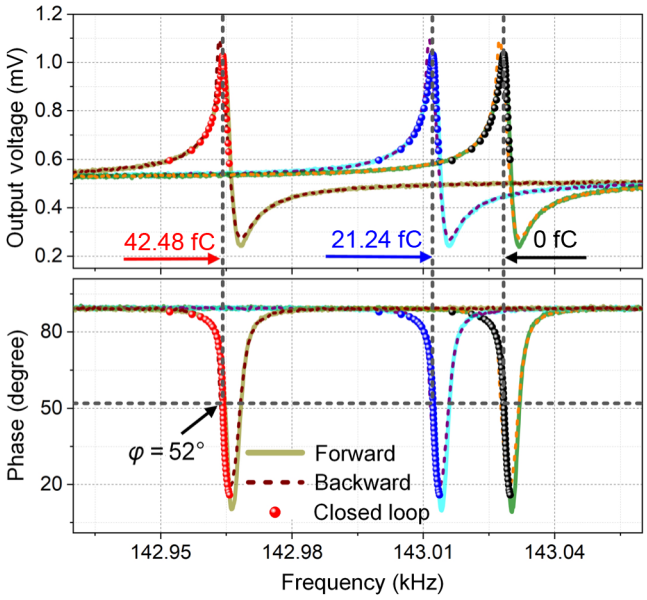

FIG. 3. Open-loop and closed-loop characterizations of the spectral response of the electrometer subject to different quantities of input charge on the gate capacitor. Dot plots are the results from closed-loop mapping and are obtained by changing the offset phase. The solid and dashed line plots are the open-loop results from frequency forward and backward sweep of a frequency response analyzer, respectively.

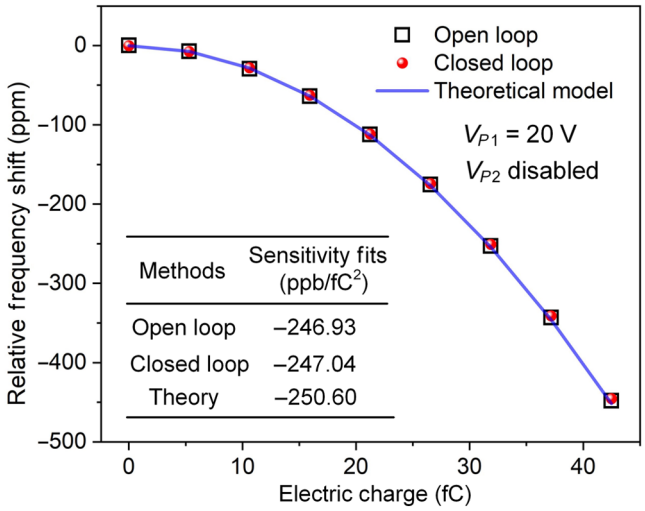

FIG. 4. Quadratic sensitivity curves of the stiffness perturbation charge-detection scheme from theoretical, open-loop and closed-loop results. The inset table shows the values of the fitted and calculated sensitivities for comparison.

with 21.24fC and 42.48fC quantities of charge applied, the frequency responses from the open-loop and closed-loop results consistently shift by −113 and −444 ppm. In particular, in the closed-loop operation, while the oscillator is operated at different locked offset phases with their corresponding oscillation amplitudes, the changes in oscillation frequencies in response to charge addition is nearly identical. This validates the functionality of charge sensing by frequency modulation within the resonance bandwidth in the stiffness perturbation scheme. As seen from the derivatives of the frequency-phase curve in Fig. 3, the noise conversions between phase to frequency are minimal at the resonance peak. The lower the noise level, the higher the resolution. Therefore, the offset phase is preferred to be locked at the resonance peak for oscillation. Thus, we keep the offset phase locked at 52° for charge measurement. The charge sensitivity at the resonance peak in closed loop is calibrated and quadratically fitted as −247.04 ppb/fC^2, as shown in Fig. 4. The sensitivity results from open-loop test and theoretical models are also plotted and summarized in the inset table where a good agreement between theoretical and experimental sensitivities can be found.

Based on the quadratic curves in Fig. 4 and with the known quantities of the prebiased charge on the gate capacitor, the frequency will change parabolically with charge addition. To verify this, we switch *S2* to V_{P2} to precharge the gate capacitor and disable V_{P1}. In this case, V_{P2} also provides polarization to the parallel-plate capacitors to enable the output of motional current during resonance. The parabolic sensitivities under four sets of preapplied Q_P from 21.24 to 42.48fC are characterized by means of open-loop and closed-loop calibration, as shown in Fig. 5 where the experimental results from open-loop and closed-loop test all match well with our theoretical predictions by Eq. (7). We further use $\gamma_P = B1 \times Q^2 + B2 \times Q$

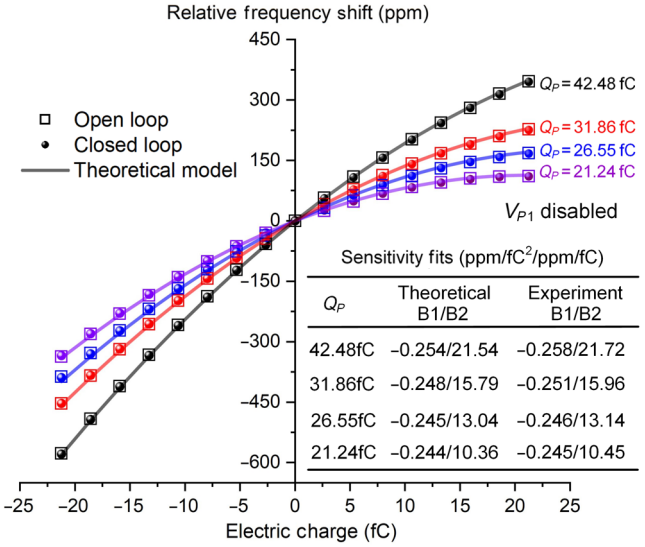

FIG. 5. Parabolic sensitivity curves of the charge prebiased scheme from theoretical model, open-loop, and closed-loop results with different quantities of preapplied Q_P for amplification. The inset table lists the parabolically fitted sensitivities of the closed-loop results and the calculated sensitivities from Eq. (7).

to fit the experimental parabolic curves from closed-loop results, as shown in the inset table of Fig. 5, together with the calculated coefficients of $B2 = -2Q_P \times B1$ and $B1 = -1/\{2\varepsilon S_C G[K_B + K_E + K_C(Q_P)]\}$ from Eq. (7). The consistency of experimental and analytical results verifies the parabolic nature of the charge sensitivity of the electrometer at prebiased states. Under different values of Q_P, the quadratic term $B1$ has values close to the original quadratic sensitivity in Fig. 4. As expected, the charge prebiased scheme mainly introduces an additional linear term $B2$ leading to sensitivity enhancement. So that, when increasing Q_P by two folds from 21.24fC, the quadratic term $B1$ is only increased by 5.3% while the linear term $B2$ is boosted by 208%. This verifies that the prebiased Q_P acts as an amplification factor to enhance the parabolic sensitivity. Within the measurement range of $\pm Q_P$, the linear term $B2$ dominates the charge sensitivity while out of that range, the quadratic term $B1$ starts to dominate. Further, the polarity of input charge is distinguished as the frequency shifts upward for measuring positive charge and shifts opposite for measuring negative charge.

Onward to the charge measurement down to electron level, the amplification by the charge prebiased scheme becomes significant and can be effectively translated into resolution enhancement. In such a context, the method of open-loop operation is impractical due to the limitations associated with sweep time and frequency accuracy as very fine frequency sweep is required. Instead, the closed-loop output is preferred for high-precision and real-time tracking of the change in oscillation frequency associated with input charge. Figure 6 plots the theoretical and closed-loop testing results of charge measurement at the electron level under the prebiased states with different Q_P required for amplification. As predicted, the experimental sensitivity curves at different prebiased states all show good linearity and agree well with the theoretical curves from our models. A ppm level of the linear frequency shift is observed regarding the input of hundreds of electrons. The experimental sensitivities are linearly fitted and summarized in the inset table, together with theoretically calculated sensitivities Γ_P from Eq. (8). The experimental sensitivity of 3.61 ppb/e under a preapplied Q_P of 42.48fC is found, which is consistent with the theoretically calculated Γ_P of 3.50 ppb/e. This clearly validates the linearized region for electron-level charge measurement that we predict in Fig. 2(d). Monitoring the linear frequency change to derive charge quantity can avoid the effect of residual charges while at the same situation, monitoring the original quadratic frequency change causes inaccurate derivation of charge quantity because the unknown quantity of residual charge on the gate functions as prebiased charge that changes the charge sensitivity. The boundaries of the linearized region are determined by the amplification of the preapplied Q_P and the nonlinear error the charge measurement can undergo. For example, for 1% affordable measurement error and a preapplied Q_P of 42.48fC, the linear region can be calculated to be ± 5310 e according to Eq. (7). Although a higher Q_P gives rise to a better electrometer performance, the prebiased scheme is limited by the pull-in effect of the capacitive transducers [37], e.g., the parallel-plate capacitors in this case.

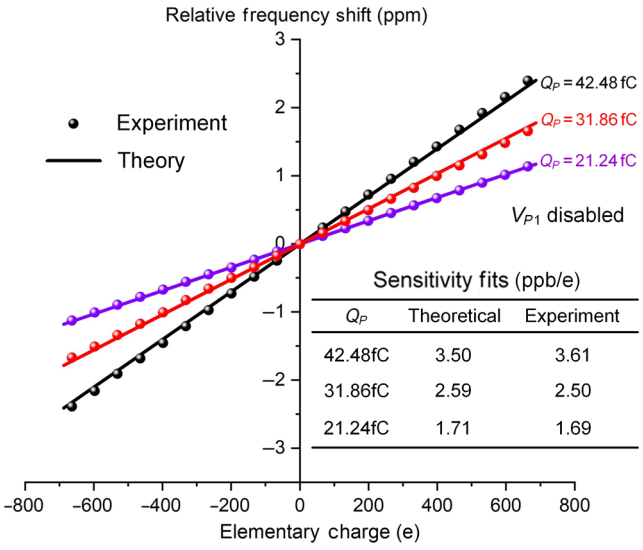

FIG. 6. Linear sensitivity curves of the charge prebiased scheme from the theoretical model and the closed-loop results under different quantities of preapplied Q_P for amplification. The inset table shows the linearly fitted sensitivities of the closed-loop results and the calculated sensitivities from Eq. (8).

IV. RESULTS AND DISCUSSION

A. Charge noise floor

In order to analyze the translation of amplification and linearization of the sensitivity into resolution enhancement, the frequency noise floor of the electrometer with and without the charge prebiased scheme are defined as $f_H(\omega)$ and $f_L(\omega)$, respectively. The charge resolution for the original stiffness perturbation scheme is given by $\Pi = [f_L(\omega)/|\Gamma|]^{1/2}$ while the enhanced resolution in the region with linearized sensitivity is given by $\Pi_P = f_H(\omega)/|\Gamma_P|$. By combining Eqs. (5) and (8), we can derive the resolution amplification factor λ as

$$\lambda = \frac{\Pi}{\Pi_P} \approx \frac{2Q_P}{\sqrt{2\varepsilon S_C G[K_B + K_E + K_C(Q_P)]}} \frac{\sqrt{f_L(\omega)}}{f_H(\omega)}. \quad (9)$$

Equation (9) can be simplified as $\lambda \approx 2Q_P \Gamma^{1/2} f_L(\omega)^{1/2}/f_H(\omega)$, which indicates that λ is proportional to the preapplied Q_P and the root square of Γ. The metrology of resonant electrometry uses frequency as the output metric, which demonstrates sensitive charge-frequency conversion and can effectively decouple charge sensing from

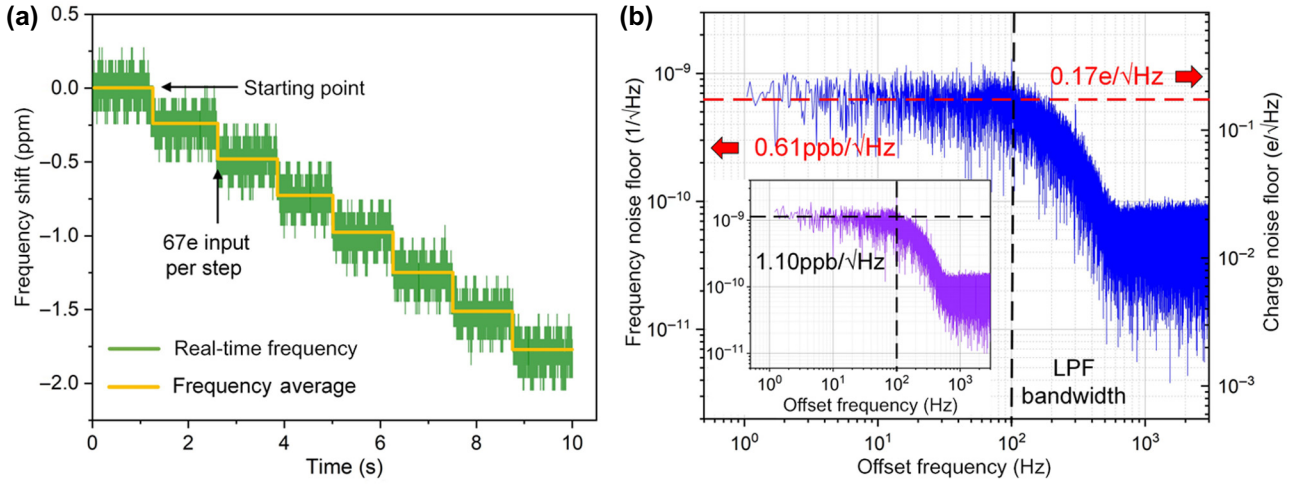

FIG. 7. (a) Real-time frequency responses of the electrometer in monitoring charge accumulation on the gate while the device is in prebiased state with Q_P of 48.41fC. The yellow line shows the averaged frequencies in a certain time period. (b) Measured frequency noise floor $f_H(\omega)$ as a function of offset frequency at the high charge-sensitive operation point corresponding to the starting point of (a). The left Y axis is the relative frequency noise floor and the right Y axis is the input-charge-referred noise-floor rescaling from the left Y axis by dividing the linearized sensitivity to intuitively show the resolution of the resonant electrometry. The inset shows the measured frequency noise floor $f_L(\omega)$ as a function of offset frequency at the low charge-sensitive operation point corresponding to the starting point of Fig. 4.

other noise sources in frequency domain. Thus, $f_H(\omega)$ and $f_L(\omega)$ mainly come from thermomechanical noise of the vibration and electronic noise of the loop. In that case, the two parameters have the same level of magnitude even though at different charge-sensitive operation points. The independence of frequency noise with respect to the charge sensitivity ensures effective translation of sensitivity amplification to the charge resolution. Detailed verification is demonstrated next.

In Fig. 7(a), the real-time frequency responses of the electrometer in monitoring charge accumulation on the gate is presented to show how frequency fluctuations influence charge detection at the electron level. With averaging of the frequency responses in a certain time period to minimize random fluctuations, we clearly observe linear frequency shift in real time in response to the charge input of 67 electrons per step, as shown by the yellow line. Accordingly, fewer electrons can be detected by tracking distinguishable smaller frequency change above the averaged random noise. Therefore, the ultimate threshold of the electron detection depends on the level of the averaged random noise, which relates to the measurement bandwidth of charge. In order to characterize the noise floor of the electrometer, the high and low charge-sensitive operation points are defined, which correspond to the operations of the device with and without the charge prebiased scheme, i.e., the operation regime on the gray area in Fig. 2(d) and on the pink area of which the charge sensitivities are given by Figs. 4 and 6, respectively. The time series data of frequency fluctuations at the high and low charge-sensitive operation points have been recorded and then processed with the fast Fourier transform to obtain the noise spectral density $f_H(\omega)$ and $f_L(\omega)$ in a broad offset frequency range, as shown in Fig. 7(b) and the inset, where the left Y axis is the frequency noise floor. The right Y axis of Fig. 7(b) is the charge-input-referred noise-floor rescaling from the left Y axis by dividing the linear sensitivity of 3.61 ppb/e. The enhanced resolution Π_P is derived as 0.17 e/$\sqrt{\text{Hz}}$ subject to a white noise level of 0.61 ppb/$\sqrt{\text{Hz}}$ obtained by the horizontal dashed line in Fig. 7(b). Notice that, there is no measurement bandwidth being applied to the charge detection, the resonant electrometer already has the ability to resolve 67 e in real time. The noise spectral density in Fig. 7(b) suggests that, by narrowing down measurement bandwidth, the frequency fluctuation in Fig. 7(a) can be reduced to achieve a better performance of real-time electron detection. For example, a time-resolved detection of a single electron requires a measurement bandwidth below 35 Hz. In comparison, the inset shows that the frequency noise floor at the low charge-sensitive operation point is 1.1 ppb/$\sqrt{\text{Hz}}$, which yields an unamplified resolution Π of 417 e/$\sqrt{\text{Hz}}$. Accordingly, the experimental value of λ is derived as 2453, which is very close to the theory of 2333 derived from Eq. (9). Experimental results prove that the frequency noise floor does not scale with the charge sensitivities of the operation points in resonant electrometry. $f_H(\omega)$ is slightly lower than $f_L(\omega)$ because the charge prebiased states increase the driving force on the transducers and the subsequent increase of the mechanical motion is beneficial for the phase noise of the oscillator and hence the frequency noise [38]. Under the charge prebiased states, the operation point corresponding to $f_H(\omega)$ is the top

TABLE I. Comparisons of the state-of-the-art electrometers at room temperature.

Year [Ref.]	Sensor type	Sensitive element	Output metric	Resolution (e/$\sqrt{\text{Hz}}$)
2004 [42]	Coulombmeter	Transistor	Analog	62 500
2014 [43]	Coulombmeter	Transistor	Analog	6250
2008 [17]	Vibrating reed	Resonator	Amplitude	6
2008 [18]	Vibrating reed	Resonator	Amplitude	52.4
2013 [19]	Vibrating reed	Resonator	Amplitude	23
2018 [20]	Vibrating reed	Resonator	Amplitude	1.03
2016 [22]	Mode localized	Resonators	Amplitude ratio	7900
2018 [23]	Mode localized	Oscillators	Amplitude ratio	9.21
2017 [27]	Resonant	Resonator	Frequency	203 000
2018 [25]	Resonant	Resonator	Frequency	16 250
2008 [24]	Resonant	Oscillator	Frequency	25 000
This Work	Resonant	Oscillator	Frequency	0.17

bifurcation point (as can be seen in our previous work [39]) in nonlinear resonance regime, which has been proved to have better noise performance than the operation points at linear regime corresponding to $f_L(\omega)$ [40]. Besides, the potential noises contributing to $f_H(\omega)$ from feedthrough effect is effectively removed by isolation of the capacitive feedthrough at the nonlinear bifurcation point by using a phase-controlled oscillation technique. Detailed demonstrations of the technique can be found in a separate study [41].

Table I lists charge resolutions of the high-end commercial instruments [42,43] and the state-of-the-art electrometers [17–20,22–25,27] that use resonators or oscillators as the core sensitive elements. A significant improvement in resolution is seen relative to other works on the resonant electrometers, and the resolution compares favorably with vibrating reed and mode-localized electrometers. The technical reasons are elaborated in the Introduction. The upper boundary of the resonant electrometry for the parabolic charge sensitivity at charge prebiased state with $Q_P = 42.48$fC is limited by the pull-in effect [37] in the gate capacitor under the input of large quantities of charge. An empirical model for predicting the pull-in limit is described in Ref. [37]. For the gate capacitor with capacitance of 1.06fF, the upper limit of charge detection is found as 770fC, which yields a dynamic range over 149 dB. Although the electrical analog electrometry systems with transistors, carbon-nanotube, quantum dots, and quantum-point contacts [6–14] generally have charge resolution at the order of 10^{-3}–10^{-6} e/$\sqrt{\text{Hz}}$ that far exceed the resolution of our device, they require extremely low temperatures and can only detect charge in the few-electrons regime. In the proposed resonant electrometry system, both high resolution and large dynamic range are achieved.

The frequency noise in the region of high offset frequency is significantly attenuated due to the use of a low-pass filter (LPF) in the control loop for frequency demodulation. The noises evident in the measurements presented in Fig. 7 are due to a combination of mechanical noise and electronic noise sources. For the mechanical noise in the oscillator, the thermomechanical noise $f(\omega)_M$ from Brownian motion is dominant, which can be estimated by [24]

$$f(\omega)_M \approx \sqrt{\frac{k_B T \Delta f}{2\pi K_B f_N Q_F A^2}}, \tag{10}$$

where k_B is the Boltzmann constant and T is the temperature. Δf is the resolution bandwidth. Q_F is the quality factor of the mechanical oscillator, the value of Q_F is derived as 50 000 by the 3-decibel method according to the spectral response in Fig. 3. Accordingly, the thermomechanical noise is estimated to be 1.76 ppt/$\sqrt{\text{Hz}}$ and this yields an ultimate threshold of the charge noise floor as 4.88×10^{-4} e/$\sqrt{\text{Hz}}$ for room-temperature resonant electrometry. The analysis on mechanical noise indicates that the resolution of the resonant electrometer is mainly dominated by the electronic noises from interface circuits. The proposed experimental prototype for resonant electrometry clearly shows extremely sensitive charge measurement with single-electron resolution. The established theoretical models also provide strategies that can further enhance the resolution of resonant electrometry for several orders of magnitude, e.g., narrowing down the gap features of the electrometer to the nanoscale, strengthening the prebiased state to move the measurement to a more sensitive region or properly integrating interface circuits on chip to minimize electronic noises.

B. Interfacing charge

When interfacing charge, three situations are considered, viz. charge loading for a single measurement, and by constant and varying charge-flow rates. We use voltage and current source to perform charge measurement at the three situations. The experimental setup is shown in Fig. 8(a). Ideally, the gate electrode should be properly insulated for preventing leakage of the input charge. In the highly doped

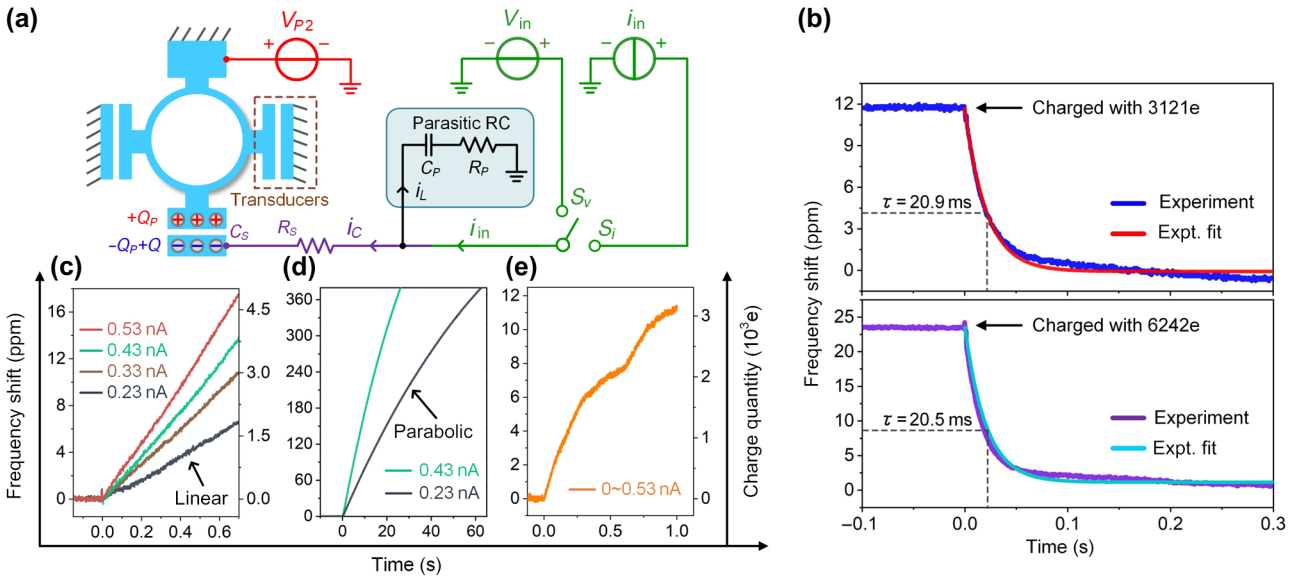

FIG. 8. (a) Experimental setup for interfacing charge on the gate. Real-time frequency output of the prototype electrometer in response to the charge loading by a single-step charge input (b), and by constant current input (c),(d) and varying currents (e). The right Y axis of (c) and (e) denote the charge quantity on the gate with the increase of time, which is rescaled from the left Y axis by dividing the experimental sensitivities of 3.61 ppb/e. For all the charge measurements the gate capacitor is prebiased by $V_{P2} = 40$ V, which corresponds to a preapplied Q_P of 42.48fC. i_C and i_L show the flows of charge accumulating on the gate and leaking through parasitic series resistance-capacitance (R_PC_P) branch.

silicon device, the resistance (R_S) at the gate is small and is negligible. However, in capacitive resonators, undesired parasitic elements are introduced, for example, the parasitic resistance (R_P) resulting from the oxide layer and the parasitic capacitance (C_P) resulting from the on-chip capacitive gaps and electrical interface circuits. Therefore, the charge at the input node leaks with a time constant defined by these parasitics. This influences electrometry performance. To perform electrometry with charge loading by one time, we switch S_v on and use voltage source $V_{\rm in}$ to charge the gate capacitor with 3121 and 6242 units of elementary charge, respectively. Then, we switch S_v off at $t = 0$ and record the frequency output of the device in time domain, as shown in Fig. 8(b). As expected, the frequency responses all follow an exponential decrease. The detection is within the regime of linear charge-frequency conversion; therefore, the Y axis is equivalent to charge quantities. Therefore, Fig. 8(b) indicates the leakage of the loaded charge on the gate electrode through the parasitic R_PC_P. In spite of the different quantities of input charge, the charge leakage has the same time constant. This is determined by discharging characteristics of the parasitic series resistance-capacitance branch, as previously noted. The time constant τ for the discharging process is found as 20.9 ms from exponential fitting, which yields $R_P \times C_P = 20.9$ ms.

Next, we switch S_i on and use current source $i_{\rm in}$ to perform charge injection on the gate electrode with constant flow rate of from 0.23–0.53 nA, respectively. As shown in Fig. 8(c), at the short time of charge injection, the frequency responses shift linearly with time increase, which corresponds to the linear sensitivity results in Fig. 6. Besides, the slope of the linear curves also changes linearly against the rate of charge injection $i_{\rm in}$, due to the fact that the charge sensitivity keeps constant even though there is simultaneous leakage (i_L) of $i_{\rm in}$ through the parasitic series resistance-capacitance branch. The charge interface circuit suggests that the ratio of the flow rate of charge leakage i_L through C_P and charge accumulation i_C on the gate capacitor C_S is independent of $i_{\rm in}$ but depends on C_P/C_S, given by $i_L/i_C = C_P/C_S$. This can be used to experimentally identify the value of C_P. For example, i_C is 4376.7 e/s at $i_{\rm in} = 0.33$ nA. Then we get $C_P/C_S = 470\,488$ for the prototype electrometer. This result is constant and can also be obtained by using other $i_{\rm in}$ in Fig. 8(c), e.g., $i_{\rm in} = 0.23, 0.43$, and 0.53 nA. For a C_S of 1.06fF in this device, C_P is estimated as 499.66pF. Such a significant parasitic capacitance is mainly from the coaxial cables used for experiments and the SOI wafer that has an embedded capacitor consisting of a 2-μm-silicon-dioxide layer sandwiched between the highly doped silicon device layers and the substrate. Further reduction of C_P can be implemented by employing a silicon-on-glass wafer [20]. In Fig. 8(d), with the longer time for charge accumulation on the gate, the frequency response eventually exhibits a parabolic nature that corresponds to the parabolic sensitivity in Fig. 5. Further, in

Fig. 8(c), we add a right *Y* axis derived by using the left *Y* axis to divide the experimental sensitivity of 3.61 ppb/e, which clearly shows the charge quantities accumulated on the gate in real time. Figure 8(e) shows the frequency output in response to the charge injection with random flow rates between 0–0.53 nA. While the device being operated in the regime with linearized charge sensitivity, the curve consists of linear branches with different slopes resulting from the different flow rates of charge injection. One advantage for measuring charge in the linear sensitive regime is that, no matter the charge input having constant or varying flow rates, the temporal frequency shift results can always reflect the variation of input charge quantity in real time, as indicated by Figs. 8(c) and 8(e), which directly demonstrate the variation of charge quantity in the right *Y* axis. Such a feature enables the proposed electrometer being directly used in monitoring the reactions in chemical ions, physical particles, and biological molecules, etc.

C. Discussion

Although the scaling laws endue the miniaturized sensors with many operational advantages, such as smaller footprint, greater sensitivity, and larger dynamic range, it also gives rise to a higher noise level, particularly for analog signals. This is the root cause that impedes the resolution of the devices with output metrics of analog [42,43] or amplitude signal [17–20,22,23] in Table I. Monitoring on the quasinature frequency from a mechanical oscillator as the sensor output is less affected by noise conversions from vibration amplitude, feedthrough [44], or other analog noise sources. Besides, the approach by precisely controlling phases in the loop for oscillation is beneficial for suppressing phase noise and thus frequency instability. Therefore, our sensing method may be instructive for developing high-performance microscopic oscillators and sensors, including providing an alternative perspective for overall loop-control strategy and leading to a change in the output metric of interest. Additionally, the highly force-sensitive mechanical oscillator in our work benefits from the scheme of stiffness perturbation that uses force to perturb modal vibration. This shows an alternative way for sensing contactless forces, which can be widely employed for measuring most of the physical quantities that can generate electric, magnetic, and inertial forces, such as magnetic and electric fields, mass and pressure, acceleration and angular rate, etc. In that case, the method of stiffness perturbation and closed-loop frequency monitoring can be developed as a common mechanism for a variety of sensors, as well as the concept of exploiting the nonlinear nature of the sensitivity for resolution enhancement.

More importantly, the micromachined electrometer can be integrated on-chip as a micromodule for embedding in the scientific instruments that requires high-precision and real-time electrometry. For example, one can use the device as a core component in a mass spectrometry system for acquiring ion information to determine elemental and isotopic signatures of a sample or to elucidate chemical composition and identity of a mixture sample. The parameters of interest in high-resolution surface imaging, such as electrostatics and short-range forces, are also measurement applications that our electrometry method focus on. This makes our method attractive for the applications in microscopy technologies, including measuring electron flow in a ballistic electron emission microscope and measuring electrostatics of the intermolecular forces for atomic force. Additionally, most of the electrical parameters, e.g., electric potential, voltage, current, can generate electrostatic force across capacitive gaps, which conforms the fundamentals of charge measurement in this work. For example, Fig. 8(c) indicates that the frequency-shift rate can be used as an output metric for measuring the input current. Therefore, with proper design of the gate capacitor, the proposed resonant electrometry implementation can be utilized as the core measurement unit to develop advanced instrumentations, such as voltmeters, ammeters, and multimeters.

V. CONCLUSION

In conclusion, we theoretically model and experimentally verify the underlying physics of the ultrasensitive resonant electrometer by tracking resonant frequency change of a built-in micromechanical oscillator with a charge-detection scheme of stiffness perturbation. We further demonstrate a charge prebiased amplification scheme for physically manipulating the quadratic charge sensitivity into a linear form with dramatic resolution enhancement over 2453 times. The experimental charge resolution is 0.17 e/$\sqrt{\text{Hz}}$. Analysis on thermomechanical noise indicates the proposed resonant electrometer has a theoretical resolution limit on the order of 10^{-4} e/$\sqrt{\text{Hz}}$. The high-performance quasidigital microscale electrometer can be employed as the core sensing element for portable and cost-effective electrometry instrumentation systems. Future work will focus on integrating interface circuits with the device for minimizing electronic noise.

ACKNOWLEDGMENTS

The authors thank Dr. Li Ding, Dr. Hao Hu, and Dr. Boran Zhang for the helpful discussions. This work is supported by the "National Natural Science Foundation of China (51875521)", the "Zhejiang Provincial Natural Science Foundation of China (LZ19E050002)" and the "Science Fund for Creative Research Groups of National Natural Science Foundation of China (51821093)".

[1] A. Menzel, A. T.-H. Lin, P. Estrela, P. Li, and A. A. Seshia, Biomolecular and electrochemical charge detection by a micromechanical electrometer, Sens. Actuators, B Chem. **160**, 301 (2011).

[2] F. Krueger and J. Larson, Chipmunk IV: Development of and experience with a new generation of radiation area monitors for accelerator applications, Nucl. Instrum. Methods Phys. Res., Sect. A **495**, 20 (2002).

[3] A. K. Naik, M. S. Hanay, W. K. Hiebert, X. L. Feng, and M. Roukes, Towards single-molecule nanomechanical mass spectrometry, Nat. Nanotechnol. **4**, 445 (2009).

[4] J. Lee, N. Tallarida, X. Chen, L. Jensen, and V. Apkarian, Microscopy with a single-molecule scanning electrometer, Sci. Adv. **4**, 5472 (2018).

[5] C. I. Callea, J. G. Mantovani, C. R. Buhler, E. E. Groop, M. G. Buehler, and A. W. Nowicki, Embedded electrostatic sensors for Mars exploration missions, Science **61**, 245 (2004).

[6] J. M. Martinis, M. Nahum, and H. D. Jensen, Metrological Accuracy of the Electron Pump, Phys. Rev. Lett. **72**, 904 (1994).

[7] R. J. Schoelkopf, P. Wahlgren, A. A. Kozhevnikov, P. Delsing, and D. E. Prober, The radio-frequency single-electron transistor (RF-SET): A fast and ultrasensitive electrometer, Science **280**, 1238 (1998).

[8] S. Gustavsson, R. Leturcq, M. Studer, T. Ihn, and K. Ensslin, Time-resolved detection of single-electron interference, Nano Lett. **8**, 2547 (2008).

[9] J. P. Pekola, O. P. Saira, V. F. Maisi, A. Kemppinen, M. Möttönen, Y. A. Pashkin, and D. V. Averin, Single-electron current sources: Toward a refined definition of the ampere, Rev. Mod. Phys. **85**, 1421 (2013).

[10] G. Podd, S. Angus, D. Williams, and A. Ferguson, Charge sensing in intrinsic silicon quantum dots, Appl. Phys. Lett. **96**, 082104 (2010).

[11] M. Biercuk, D. Reilly, T. Buehler, V. Chan, J. Chow, R. Clark, and C. Marcus, Charge sensing in carbon-nanotube quantum dots on microsecond timescales, Phys. Rev. B **73**, 201402 (2006).

[12] D. Reilly and C. Marcus, Fast single-charge sensing with a rf quantum point contact, Appl. Phys. Lett. **91**, 162101 (2007).

[13] B. J. van Wees, H. van Houten, C. Beenakker, J. G. Williamson, L. Kouwenhoven, and D. van der Marel, Quantized Conductance of Point Contacts in a Two-Dimensional Electron Gas, Phys. Rev. Lett. **60**, 848 (1988).

[14] I. Ahmed, J. A. Haigh, S. Schaal, S. Barraud, Y. Zhu, Ch. Lee, M. Amado, J. W. A. Robinson, A. Rossi, J. J. L. Morton, and M. F. Gonzalez-Zalba, Radio-Frequency Capacitive Gate-Based Sensing, Phys. Rev. Appl. **10**, 014018 (2018).

[15] A. N. Cleland and M. L. Roukes, A nanometre-scale mechanical electrometer, Nature **392**, 160 (1998).

[16] P. Häkkinen, A. Isacsson, A. Savin, J. Sulkko, and P. Hakonen, Charge sensitivity enhancement via mechanical oscillation in suspended carbon nanotube devices, Nano Lett. **15**, 1667 (2015).

[17] J. Lee, Y. Zhu, and A. Seshia, Room temperature electrometry with sub-10 electron charge resolution, J. Micromech. Microeng. **18**, 025033 (2008).

[18] Y. Zhu, J. Lee, and A. Seshia, A resonant micromachined electrostatic charge sensor, IEEE Sens. J. **8**, 1499 (2008).

[19] G. Jaramillo, C. Buffa, M. Li, F. J. Brechtel, G. Langfelder, and D. A. Horsley, MEMS electrometer With femtoampere resolution for aerosol particulate measurements, IEEE Sens. J. **13**, 2993 (2013).

[20] J. Jalil, Y. Ruan, and Y. Zhu, Room-Temperature sensing of single electrons using vibrating-reed electrometer in silicon-on-glass technology, IEEE Electron Device Lett. **39**, 1928 (2018).

[21] P. Thiruvenkatanathan, J. Yan, and A. Seshia, in *Proceedings of the IEEE International Frequency Control Symposium* (2010), pp. 91–96.

[22] H. Zhang, J. Huang, W. Yuan, and H. Chang, A high-sensitivity micromechanical electrometer based on mode localization of Two degree-of-freedom weakly coupled resonators, J. Microelectromech. Syst. **25**, 937 (2016).

[23] J. Yang, H. Kang, and H. Chang, in *Proceedings of the IEEE 31st Micro Electro Mechanical Systems (MEMS 2018)* (2018), pp. 67–70.

[24] J. Lee, B. Bahreyni, and A. A. Seshia, An axial strain modulated double-ended tuning fork electrometer, Sens. Actuators, A Phys. **148**, 395 (2008).

[25] D. Chen, J. Zhao, Y. Wang, Zh. Xu, and J. Xie, Sensitivity manipulation on micro-machined resonant electrometer toward high resolution and large dynamic range, Appl. Phys. Lett. **112**, 013502 (2018).

[26] D. Chen, J. Zhao, Zh. Xu, and J. Xie, A micro resonant charge sensor with enhanced sensitivity based on differential sensing scheme and leverage mechanisms, AIP Adv. **6**, 105106 (2016).

[27] D. Chen, J. Zhao, Y. Wang, and J. Xie, An electrostatic charge sensor based on micro resonator with sensing scheme of effective stiffness perturbation, J. Micromech. Microeng. **27**, 065002 (2017).

[28] H. Zhang, J. Yang, W. Yuan, and H. Chang, Linear sensing for mode-localized sensors, Sens. Actuator A Phys. **277**, 35 (2018).

[29] H. Zhang, H. Kang, and H. Chang, Suppression on nonlinearity of mode-localized sensors using algebraic summation of amplitude ratios as the output metric, IEEE Sens. J. **18**, 7802 (2018).

[30] J. M. L. Miller, H. Zhu, D. B. Heinz, Y. Chen, I. B. Flader, D. D. Shin, J. E.-Y. Lee, and T. W. Kenny, Thermal-Piezoresistive Tuning of the Effective Quality Factor of a Micromechanical Resonator, Phys. Rev. Appl. **10**, 044055 (2018).

[31] X. Zhou, D. Xiao, X. Wu, Q. Li, Z. Hou, K. He, and Y. Wu, Mitigating Thermoelastic Dissipation of Flexural Micromechanical Resonators by Decoupling Resonant Frequency From Thermal Relaxation Rate, Phys. Rev. Appl. **8**, 064033 (2017).

[32] L. Laurent, J. Yon, J. Moulet, M. Roukes, and L. Duraffourg, 12-μm-Pitch Electromechanical Resonator for Thermal Sensing, Phys. Rev. Appl. **9**, 024016 (2018).

[33] D. Chen, J. Sun, M. Pandit, G. Sobreviela, X. Chen, A. Seshia, and J. Xie, in *Proceedings of the International Conference on Solid-State Sensors, Actuators and Microsystems & Eurosensors* (2019), pp. 2091–2094.

[34] D. Chen, Y. Wang, X. Chen, L. Yang, and J. Xie, Temperature-frequency drift suppression via electrostatic stiffness softening in MEMS resonator with weakened duffing nonlinearity, Appl. Phys. Lett. **114**, 023502 (2019).

[35] D. Chen, Y. Wang, Y. Guan, X. Chen, X. Liu, and J. Xie, Methods for nonlinearities reduction in micromechanical beams resonators, J. Microelectromech. Syst. **27**, 764 (2018).

[36] M. Sansa, E. Sage, E. Bullard, M. Gély, T. Alava, E. Colinet, A. Naik, L. Villanueva, L. Duraffourg, M. Roukes, G. Jourdan, and S. Hentz, Frequency fluctuations in silicon nano-resonators, Nat. Nanotechnol. **11**, 552 (2016).

[37] Chang, Liu. *Chapter 4 of Foundations of MEMS.* (Pearson/Prentice Hall, 2011).

[38] L. Villanueva, E. Kenig, R. Karabalin, M. Matheny, Ron Lifshitz, M. Cross, and M. Roukes, Surpassing Fundamental Limits of Oscillators Using Nonlinear Resonators, Phys. Rev. Lett. **110**, 177208 (2013).

[39] D. Chen, H. Zhang, J. Sun, M. Pandit, G. Sobreviela, Y. Wang, Q. Zhang, X. Chen, A. Seshia, and J. Xie, in *Proceedings of the IEEE 33rd International Conference on Micro Electro Mechanical Systems (MEMS 2020)* (2020), pp. 182–185.

[40] G. Sobreviela, C. Zhao, M. Pandit, C. Do, S. Du, X. Zou, and A. A. Seshia, Parametric noise reduction in a high-order nonlinear MEMS resonator utilizing its bifurcation points, J. Microelectromech. Syst. **26**, 1189 (2017).

[41] D. Chen, H. Zhang, J. Sun, M. Pandit, G. Sobreviela, Y. Wang, Q. Zhang, X. Chen, A. Seshia, and J. Xie, in *Proceedings of the IEEE 33rd International Conference on Micro Electro Mechanical Systems (MEMS 2020)* (2020), pp. 773–776.

[42] Low Level Measurements Handbook, Keithley Instrum., Cleveland, OH, USA, 2004. Accessed: Feb. 21, 2016.

[43] Keysight Technology. B2980 Series Femto/Picoammeter Electrometer/High Resistance Meter. Accessed: Sep. 28, 2018.

[44] J. Lee and A. A. Seshia, Direct parameter extraction in feedthrough-embedded capacitive MEMS resonators, Sens. Actuator A Phys. **167**, 237 (2011).